ANIMAL ROBOTS

A biomimetic robotic platform to study flight specializations of bats

Alireza Ramezani,[1] Soon-Jo Chung,[2]* Seth Hutchinson[1]

Bats have long captured the imaginations of scientists and engineers with their unrivaled agility and maneuvering characteristics, achieved by functionally versatile dynamic wing conformations as well as more than 40 active and passive joints on the wings. Wing flexibility and complex wing kinematics not only bring a unique perspective to research in biology and aerial robotics but also pose substantial technological challenges for robot modeling, design, and control. We have created a fully self-contained, autonomous flying robot that weighs 93 grams, called Bat Bot (B2), to mimic such morphological properties of bat wings. Instead of using a large number of distributed control actuators, we implement highly stretchable silicone-based membrane wings that are controlled at a reduced number of dominant wing joints to best match the morphological characteristics of bat flight. First, the dominant degrees of freedom (DOFs) in the bat flight mechanism are identified and incorporated in B2's design by means of a series of mechanical constraints. These biologically meaningful DOFs include asynchronous and mediolateral movements of the armwings and dorsoventral movements of the legs. Second, the continuous surface and elastic properties of bat skin under wing morphing are realized by an ultrathin (56 micrometers) membranous skin that covers the skeleton of the morphing wings. We have successfully achieved autonomous flight of B2 using a series of virtual constraints to control the articulated, morphing wings.

INTRODUCTION

Biologically inspired flying robots showcase impressive flight characteristics [e.g., robot fly (1) and bird-like robots (2, 3)]. In recent years, biomimicry of bat flight has led to the development of robots that are capable of mimicking bat morphing characteristics on either a stationary (4) or a rotational pendular platform (5). However, these attempts are limited because of the inherent complexities of bat wing morphologies and lightweight form factors.

Arguably, bats have the most sophisticated powered flight mechanism among animals, as evidenced by the morphing properties of their wings. Their flight mechanism has several types of joints (e.g., ball-and-socket and revolute joints), which interlock the bones and muscles to one another and create a metamorphic musculoskeletal system that has more than 40 degrees of freedom (DOFs), both passive and active (see Fig. 1) (6). For insects, the wing structure is not as sophisticated as bats because it is a single, unjointed structural unit. Like bat wings, bird wings have several joints that can be moved actively and independently.

Robotics research inspired by avian flight has successfully conceptualized bird wings as a rigid structure, which is nearly planar and translates—as a whole or in two to three parts—through space; however, the wing articulation involved in bat wingbeats is very pronounced. In the mechanism of bat flight, one wingbeat cycle consists of two movements: (i) a downstroke phase, which is initiated by both left and right forelimbs expanding backward and sideways while sweeping downward and forward relative to the body, and (ii) an upstroke phase, which brings the forelimbs upward and backward and is followed by the flexion of the elbows and wrists to fold the wings. There are more aspects of flapping flight that uniquely distinguish bats. Bat wings have (i) bones that deform adaptively during each wingbeat cycle, (ii) anisotropic wing membrane skin with adjustable stiffness across the

wing, and (iii) a distributed network of skin sensory organs believed to provide continuous information regarding flows over the wing surfaces (7).

The motivation for our research into bat-inspired aerial robots is twofold. First, the study of these robots will provide insight into flapping aerial robotics, and the development of these soft-winged robots will have a practical impact on robotics applications where humans and robots share a common environment. From an engineering perspective, understanding bat flight is a rich and interesting problem. Unlike birds or insects, bats exclusively use structural flexibility to generate the controlled force distribution on each membrane wing. Wing flexibility and complex wing kinematics are crucial to the unrivaled agility of bat flight (8, 9). This aspect of bat flight brings a unique perspective to research in winged aerial robotics, because most previous work on bioinspired flight is focused on insect flight (10–15) or hummingbird flight (16), using robots with relatively stiff wings (17, 18).

Bat-inspired aerial robots have a number of practical advantages over current aerial robots, such as quadrotors. In the case of humans and robots co-inhabiting shared spaces, the safety of bat-inspired robots with soft wings is the most important advantage. Although quadrotor platforms can demonstrate agile maneuvers in complex environments (19, 20), quadrotors and other rotorcraft are inherently unsafe for humans; demands of aerodynamic efficiency prohibit the use of rotor blades or propellers made of flexible material, and high noise levels pose a potential hazard for humans. In contrast, the compliant wings of a bat-like flapping robot flapping at lower frequencies (7 to 10 Hz versus 100 to 300 Hz of quadrotors) are inherently safe, because their wings comprise primarily flexible materials and are able to collide with one another, or with obstacles in their environment, with little or no damage.

Versatile wing conformation

The articulated mechanism of bats has speed-dependent morphing properties (21, 22) that respond differently to various flight maneuvers. For instance, consider a half-roll (180° roll) maneuver performed by

[1]Coordinated Science Laboratory, University of Illinois at Urbana-Champaign, Urbana, IL 61801, USA. [2]Graduate Aerospace Laboratories, California Institute of Technology, Pasadena, CA 91125, USA.
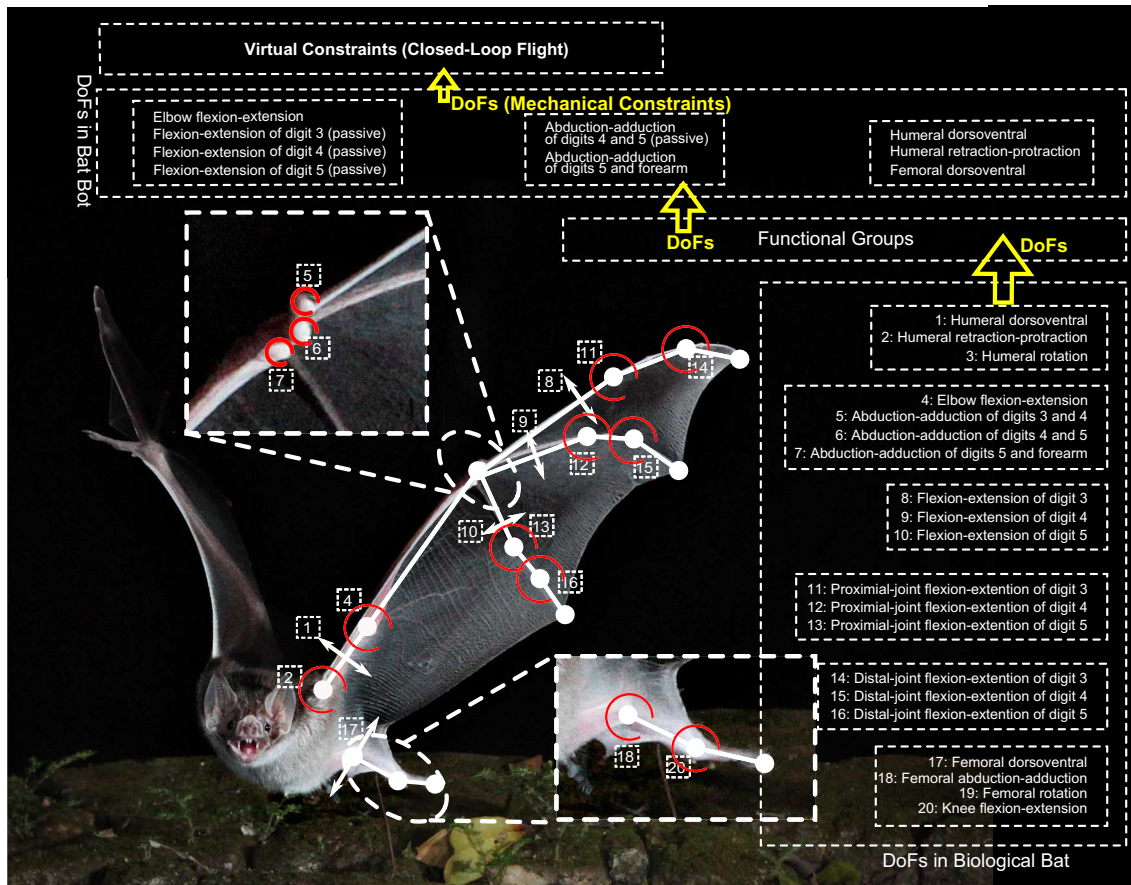*Corresponding author. Email: sjchung@caltech.edu

Fig. 1. Functional groups in bat (photo courtesy of A. D. Rummel and S. Swartz, the Aeromechanics and Evolutionary Morphology Laboratory, Brown University). Enumerated bat joint angles and functional groups are depicted; using these groups makes it possible to categorize the sophisticated movements of the limbs during flight and to extract dominant DOFs and incorporate them in the flight kinematics of B2. The selected DOFs are coupled by a series of mechanical and virtual constraints.

insectivorous bats (23). Flexing a wing and consequently reducing the wing area would increase wing loading on the flexed wing, thereby reducing the lift force. In addition, pronation (pitch-down) of one wing and supination (pitch-up) of the other wing result in negative and positive angles of attack, respectively, thereby producing negative and positive lift forces on the wings, causing the bat to roll sharply. Bats use this maneuver to hunt insects because at 180° roll, they can use the natural camber on their wings to maximize descending acceleration. Insectivorous bats require a high level of agility because their insect preys are also capable of swooping during pursuit. With such formidable defense strategies used by their airborne prey, these bats require sharp changes in flight direction.

In mimicking bats' functionally versatile dynamic wing conformations, two extreme paradigms are possible. On the one hand, many active joints can be incorporated in the design. This school of thought can lead to the design and development of robots with many degrees of actuation that simply cannot fly. Apart from performance issues that may appear from overactuating a dynamic system, these approaches are not practical for bat-inspired micro aerial vehicles (MAVs) because there are technical restrictions for sensing and actuating many joints in robots with tight weight (less than 100 g) and dimension restrictions. On the other hand, oversimplifying the morphing wing kinematics to oscillatory flat surfaces, which is similar to conventional ornithopters, underestimates the complexities of the bat flight mechanism. Such

simplified ornithopters with simple wing kinematics may not help answer how bats achieve their impressive agile flight.

Body dimensional complexity

A better understanding of key DOFs in bat flight kinematics may help to design a simpler flying robot with substantially fewer joints that is yet capable of mimicking its biological counterparts. A similar paradigm has led to successful replications of the human terrestrial locomotion (walking and running) by using bipedal robots that have point feet (24), suggesting that feet are a redundant element of the human locomotion system. Assigning importance to the kinematic parameters can yield a simpler mechanism with fewer kinematic parameters if those parameters with higher kinematic contribution and significance are chosen. Such kinematic characterization methods have been applied to study various biological mechanisms (6, 9, 25–28).

Among these studies, Riskin et al. (6) enhance our understanding of bat aerial locomotion in particular by using the method of principal components analysis (PCA) to project bat joint movements to the subspace of eigenmodes, isolating the various components of the wing conformation. By using only the first eigenmode, 34% of biological bat flight kinematics are reproducible. By superimposing the first and second eigenmodes, more than 57% of bat flight kinematics can be replicated. These findings, which emphasize the existence of synergies (29) in bat flight kinematics to describe the sophisticated movements of the
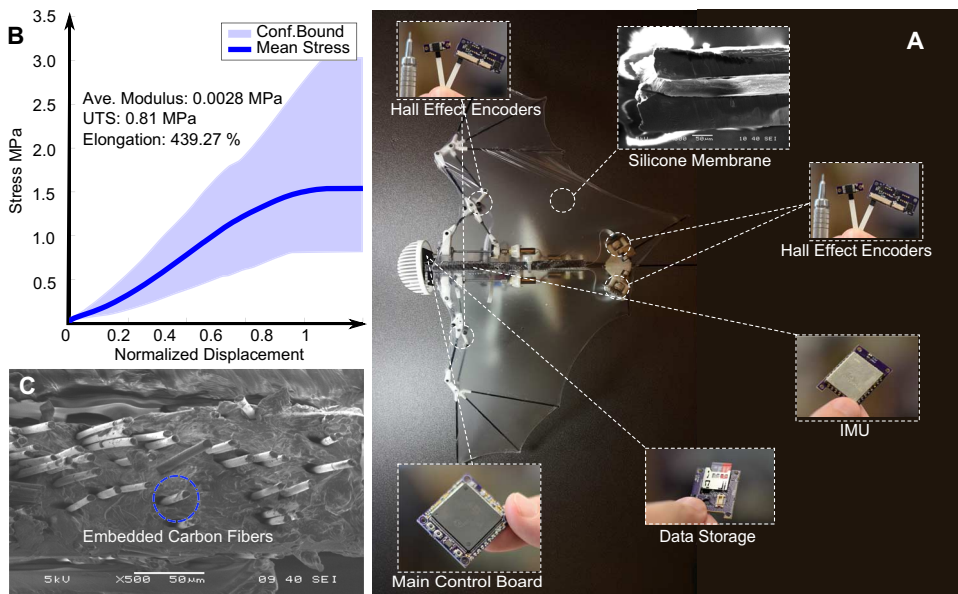
Fig. 2. Bat Bot. (**A**) B2 is self-sustained and self-contained; it has an onboard computer and several sensors for performing autonomous navigation in its environment. The computing, sensing, and power electronics, which are accommodated within B2, are custom-made and yield a fully self-sustained system despite weight and size restrictions. The computing unit, or main control board (MCB), hosts a microprocessor. While the navigation-and-control algorithm runs on the MCB in real time, a data acquisition unit acquires sensor data and commands the micro actuators. The sensing electronics, which are circuit boards custom-designed to achieve the smallest size possible, interface with the sensors and the MCB by collecting two kinds of measurements. First, an inertial measurement unit (IMU), which is fixed to the ribcage in such a way that the x axis points forward and the z axis points upward, reads the attitudes of the robot with respect to the inertial frame. Second, five magnetic encoders are located at the elbows, hips, and flapping joint to read the relative angles between the limbs with respect to the body. (**B**) Dynamic modulus analysis. Samples of membrane were mounted vertically in the dynamic modulus analyzer using tension clamps with ribbed grips to ensure that there was no slipping of the sample. Data were collected using controlled force analysis at a ramp rate of 0.05 N/min over the range 0.001 to 1.000 N. The temperature was held at 24.56°C. The estimated average modulus, ultimate tensile strength (UTS), and elongation are 0.0028 MPa, 0.81 MPa, and 439.27%, respectively. The average modulus and UTS along fiber direction are 11.33 and 17.35 MPa, respectively. (**C**) The custom-made silicone-based membrane and embedded carbon fibers.

limbs during flight, suggest the possibility of mimicking bat kinematics with only a few DOFs (*30*).

According to these PCAs, three functional groups, shown in Fig. 1, synthesize the wing morphing: (i) when wings spread, fingers bend; (ii) when wrists pronate, elbows bend; and (iii) the medial part of the wings is morphed in collaboration with the shoulders, hips, and knees (*6*). These dimensional complexity analyses reveal that the flapping motion of the wings, the mediolateral motion of the forelimbs, the flexion-extension of the fingers, the pronation-supination of the carpi, and the dorsoventral movement of the legs are the major DOFs. In developing our robotic platform Bat Bot (B2) (Fig. 2A), we selected these biologically meaningful DOFs and incorporated them in the design of B2 by means of a series of mechanical constraints.

RESULTS

System design

B2's flight mechanism (shown in Fig. 3, A to C) consists of the left and right wings, each including a forelimb and a hindlimb mechanism. The left and right wings are coupled with a mechanical oscillator. A motor spins a crankshaft mechanism, which moves both wings synchronously dorsoventrally while each wing can move asynchronously

mediolaterally. The hindlimbs that synthesize the trailing edge of the wings can move asynchronously and dorsoventrally. If it were not for mechanical couplings and constraints, the morphing mechanism of B2 would have nine DOFs. Because the physical constraints are present, four DOFs are coupled, yielding a five-DOF mechanism.

The forelimbs (see Fig. 3B), which provide membranal mechanical support and morphing leverage, consist of nine links: the humeral (p_0-p_1), humeral support (p_1-p_2), radial (p_1-p_3), radial support (p_4-p_5), carpal (p_3-p_4), carpal support (p_1-p_5), and three digital links. Mobilizing this structure requires embedding rotation in the humerus, pronating rotation in the wrists, and abduction-adduction and flexion-extension in the digits. All of these require the active actuation of the shoulders, wrists, and finger knuckles, respectively.

A few attempts have been made to incorporate similar DOFs in an MAV. Researchers at Brown University have used string-and-pulley–based actuating mechanisms to articulate a robotic membranous wing (*4*). In their design, the wing is mounted on a support to avoid any installation of actuators on the robotic wing. In this support, a bundle that includes several strings is routed through the wing's links. It is then connected to several motors incorporated in the support. This form of actuation makes it possible to realize several active joints in the robotic wing. However, such a method is not practical for a flying MAV because it requires heavy actuators to be installed in the ribcage. Unlike the robotic wing from (*4*), we introduced physical constraints (see Fig. 3, A to C) in B2 to synthesize a flight mechanism with a few actuated joints. These mechanical constraints follow.

Morphing wing flight apparatus

A three-link mechanism, where each link is connected to the next one with a revolute joint while one link is pivoted to a fixed support, is uniquely defined mathematically using three angles or configuration variables. Regulating the position and orientation of the end effector in the three-link mechanism implies direct control of the three revolute joints. Constraining the mechanism with three rigid links results in a one-DOF mechanism requiring only one actuator.

Each of the forelimbs is similar to this three-link mechanism, and their links are hinged to one another using rigid one-DOF revolute joints. The rotational movement of the humeral link around the fixed shoulder joint p_0 is affected by linear movements of the point p_2 relative to the humeral shoulder joint. A linear motion of the humeral support link at the shoulder moves the radial link relative to the humeral link and results in elbow flexion-extension. Although humeral and radial links move with respect to each other, a relative motion of the outer digital link with respect to the radial link is realized as
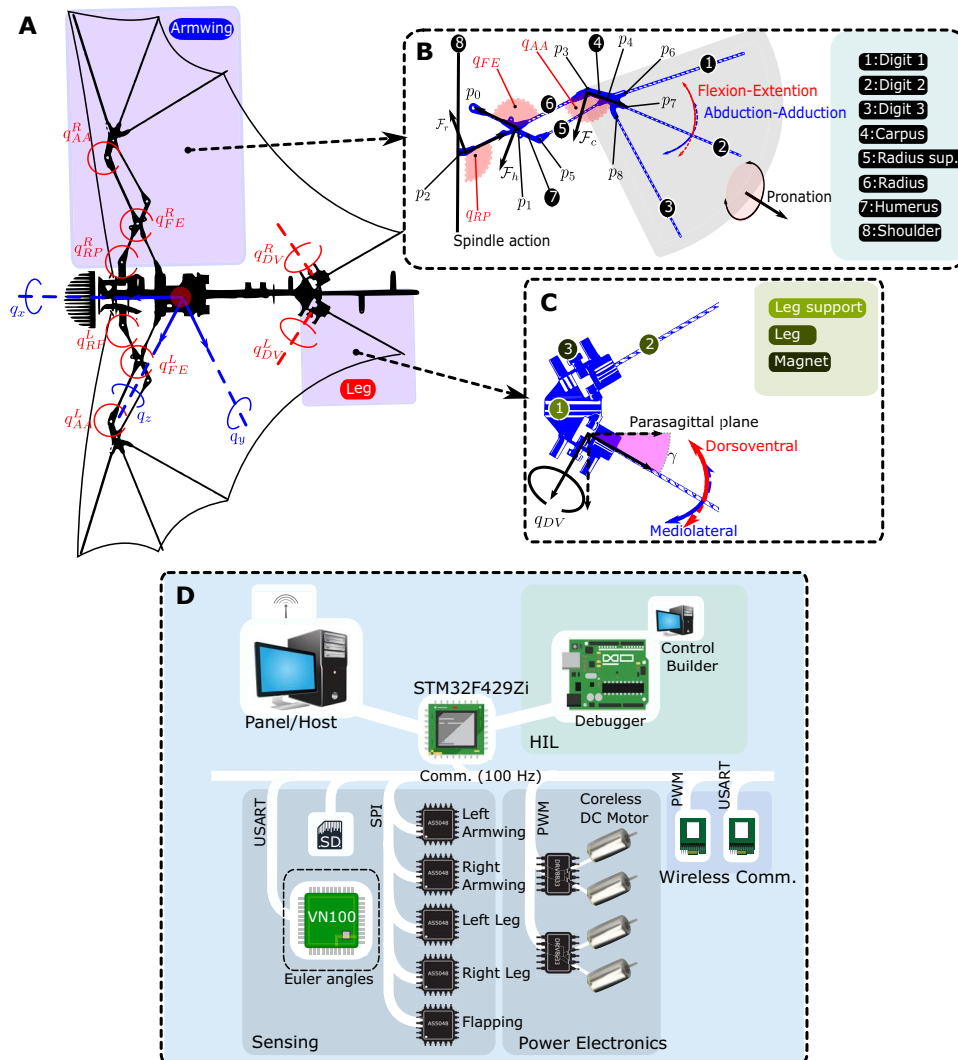
Fig. 3. Mechanism and electronics overview. (**A**) B2's flight mechanism and its DOFs. We introduced mechanical couplings in the armwing to synthesize a mechanism with a few DOFs. (**B**) The armwing retains only one actuated movement, which is a push-pull movement produced by a spindle mechanism hosted in the shoulder. (**C**) The leg mechanism. (**D**) B2's electronics architecture. At the center, the microprocessor from STMicroelectronics communicates with several components, including an IMU from VectorNav Technologies, an SD card reader, five AS5048 Hall effect encoders, and two dual-port dc motor drivers. Two wireless communication devices, an eight-channel micro RC receiver (DSM2) and a Bluetooth device, make it possible to communicate with the host (Panel). The microprocessor has several peripherals, such as universal synchronous/asynchronous receiver/transmitter (USART), serial peripheral interface (SPI), pulse-width modulation (PWM), and secure digital input/output (SDIO). To test and deploy the controller on the platform, we used Hardware-in-the-Loop (HIL) simulation. In this method, a real-time computer is used as a virtual plant (model), and the flight controller, which is embedded on the physical microprocessor, responds to the state variables of the virtual model. In this way, the functionality of the controller is validated and debugged before being deployed on the vehicle.

the elbow flexion-extension is projected to the carpal plate through the radial support link (see Fig. 3B).

The ball-and-socket universal joints at two ends of the support radial link facilitate the passive movements of the carpal plate in a pronating direction. In contrast to biological bats, which actively rotate their wrists, B2 has passive carpal rotations with respect to the radius.

Digital links I, II, and III are cantilevered to the carpal plate (p_6, p_7, and p_8); they are flexible slender carbon fiber tubes that can passively flex and extend with respect to the carpal plate, meaning that they in-

troduce passive DOFs in the flight mechanism. In addition to these passive flexion-extension movements, the digital links can passively abduct and adduct with respect to each other. The fingers have no knuckles, and their relative angle with respect to one another is predefined.

As a result, each of B2's forelimbs has one actuated DOF that transforms the linear motion of its spindle mechanism into three active and biologically meaningful movements: (i) active humeral retraction-protraction (shoulder angle), (ii) active elbow flexion-extension (elbow angle), and (iii) active carpal abduction-adduction (wrist angle). The passive DOFs include carpal pronation, digital abduction-adduction, and flexion-extension.

In the case of the hindlimbs (legs), it is challenging to accurately quantify the aerodynamic consequences of leg absence or presence in bats and determine their influence on the produced aerodynamic lift and drag forces. This is because the movements of hindlimbs affect the membrane locally at the trailing edge of the wings, whereas at distal positions, wings are mostly influenced by forelimbs. However, legs can enhance the agility of flight by providing additional control of the left and right sides of the trailing edge of the membrane wing (31). Adjusting the vertical position of the legs with respect to the body has two major effects: (i) leg-induced wing camber and (ii) increasing the angle of attack locally at the tail. In other words, increasing the leg angle increases lift, drag, and pitching moment (31). In addition, there is another benefit to carefully controlled tail actuation: Drag notably decreases because tails prevent flow detachments and delay the onset of flow separation (32).

Benefiting from these aerodynamic effects, bats have unique mechanistic bases; the anatomical evolutions in their hindlimbs enable these mammals to actively use their hindlimbs during flight (33). In contrast to terrestrial mammals, the ball-and-socket joint that connects the femoral bone to the body is rotated in such a way that knee flexion moves the ankle dorsoventrally. This condition yields pronounced knee flexions ventrally.

From a kinematics standpoint, the sophisticated movements of ankles in bats include dorsoventral and mediolateral movements. Ankles move ventrally during the downstroke, and they start moving dorsally during the upstroke (33). Motivated by the roles of legs in bat flight, we implemented two asynchronously active legs for controlling the trailing edge of the membrane wing in the design of B2. We

hinged each leg to the body by one-DOF revolute joints such that the produced dorsoventral movement happens in a plane that is tilted at an angle relative to the parasagittal plane (see Fig. 3C). Contrary to biological bats, B2's legs have no mediolateral movements; Riskin *et al.* (*6*) suggest that such movements are less pronounced in biological bats. To map the linear movements of our actuation system to the dorsoventral movements of the legs, we used a three-bar linkage mechanism (*34*).

Anisotropic membranous wing

The articulated body of B2 yields a structure that cannot accommodate conventional fabric covering materials, such as unstretchable nylon films. Unstretchable materials resist the forelimb and leg movements. As a result, we covered the skeleton of our robot with a custom-made, ultrathin (56 μm), silicone-based membrane that is designed to match the elastic properties of biological bats' membranes. In general, bat skin spans the body such that it is anchored to forelimbs, digital bones, and hindlimbs. This yields a morphing mechanism with soft wings, which is driven by the movements of the limbs. These compliant and anisotropic structures with internal tensile forces in dorsoventral and mediolateral directions have elastin fiber bundles, which provide an extensibility and self-folding (self-packing) property to the wing membrane (*35*).

Reverse engineering all of these characteristics is not feasible from an engineering fabrication standpoint; therefore, we focused our attention on a few properties of the membrane wing. In producing such a membranous wing, we studied the anatomical properties of bats' biological skin and found the key features to be (i) weight per unit of area (area density), (ii) tensile modulus, and (iii) stretchability (see Fig. 2, B and C). The area density is important because high-density membranes distributed across the robot's skeleton increase the wing's moment of inertia along the flapping axis and the overall payload of B2. In addition, internal tensile forces introduced by the membrane to the system are important because the micro motors used in the robot have limited torque outputs. When the pretension forces become large, the stall condition emerges in the actuators. This can damage the motor as well as the power electronics. The stretchability of the membrane defines the capacity of the wing to fold and unfold mediolaterally within the range of movement of actuators so that undesirable skin wrinkles or ruptures are avoided.

To produce an ultrathin and stretchable skin, we used two ultraflat metal sheets with a 10-μm flatness precision to sandwich our silicone materials. This ensures an even and consistent pressure distribution profile on the material. We synthesized a polymer in which two components—one containing a catalyst and the other containing polyorganosiloxanes with hydride functional groups—began vulcanization in the laboratory environment. The first component is a mixture of 65 to 75% by weight polyorganosiloxanes and 20 to 25% amorphous silica, and the second component is a mixture of 75 to 85% polyorganosiloxanes, 20 to 25% amorphous silica, and less than 0.1% platinum-siloxane complex. Platinum-siloxane is a catalyst for polymer chain growth. The Si–O bond length is about 1.68 Å with a bond angle of 130°, whereas the C–C bond found in most conventional polymers is about 1.54 Å with a 112° bond angle. Because of these geometric factors, silicone polymers exhibit a greater percentage of elongation and flexibility than carbon backbone polymers. However, silica is heavier than carbon, which could potentially make the wing too heavy and too rigid for flight. To solve this problem, we added hexamethyldisiloxane, which reduces the thickness and viscosity of the silicone, in an experimentally determined ratio.

Virtual constraints and feedback control

A crucial but unseen component of B2 is its flight control supported by its onboard sensors, high-performance micromotors with encoder feedback, and a microprocessor (see Fig. 3D). B2 and conventional flying robots such as fixed-wing and rotary-wing robots are analogous in that they all rely on oscillatory modulations of the magnitude and direction of aerodynamic forces. However, their flight control schemes are different. Conventional fixed-wing MAVs are often controlled by thrust and conventional control surfaces such as elevators, ailerons, and rudders. In contrast, B2 has nine active oscillatory joints (five of which are independent) in comparison to six DOFs (attitude and position) that are actively controlled. In other words, the control design requires suitable allocation of the control efforts to the joints.

In addition, challenges in flight control synthesis for B2 have roots in the nonlinear nature of the forces that act on it. B2, similar to fruit bats in size and mass (wing span, 30 to 40 cm; mass, 50 to 150 g), is capable of achieving a flapping frequency that is lower than or equal to its natural body response; as a result, it is often affected by nonlinear inertial and aerodynamic artifacts. Such forces often appear as nonlinear and nonaffine in-control terms in the equations of motion (*36*). Therefore, conventional approximation methods that assume flapping frequency to be much faster than the body dynamic response, such as the celebrated method of averaging, commonly applied to insect-scale flapping flight (*10*, *11*), fail to make accurate predictions of the system's behavior.

The approach taken in this paper is to asymptotically impose virtual constraints (holonomic constraints) on B2's dynamic system through closed-loop feedback. This concept has a long history, but its application in nonlinear control theory is primarily due to the work of Isidori *et al.* (*37*, *38*). The advantage of imposing these constraints through closed-loop feedback (software) rather than physically (hardware) is that B2's wing configurations can be adjusted and modified during the flight. We have tested this concept on B2 to generate cruise flights, bank turning, and sharp diving maneuvers, and we anticipate that this can potentially help reconstruct the adaptive properties of bat flight for other maneuvers. For instance, bats use tip reversal at low flight speeds (hovering) to produce thrust and weight support, and the stroke plane becomes perpendicular to the body at higher flight speeds (*39*).

We parameterized the morphing structure of B2 by several configuration variables. The configuration variable vector $\mathbf{q}_{morph}$, which defines the morphology of the forelimb and hindlimb as they evolve through the action of actuated coordinates, embodies nine biologically meaningful DOFs

$$\mathbf{q}_{morph} = (q_{RP}^R; q_{FE}^R; q_{AA}^R; q_{DV}^R; q_{RP}^L; q_{FE}^L; q_{AA}^L; q_{DV}^L; q_{FL}) \qquad (1)$$

where q_{RP}^i describes the retraction-protraction angle, q_{FE}^i is the radial flexion-extension angle, q_{AA}^i is the abduction-adduction angle of the carpus, q_{FL} is the flapping angle, and q_{DV}^i is the dorsoventral movement of the hindlimb (see Fig. 3, B and C). Here, the superscript i denotes the right (R) or left (L) joint angles. The mechanical constraints described earlier yield a nonlinear map from actuated joint angles

$$\mathbf{q}_{act} = (y_{spindle}^R; q_{DV}^R; y_{spindle}^L; q_{DV}^L; q_{FL}) \qquad (2)$$

to the morphology configuration variable vector $\mathbf{q}_{morph}$. The spindle action shown in Fig. 3B is denoted by $y_{spindle}^i$. The nonlinear map is
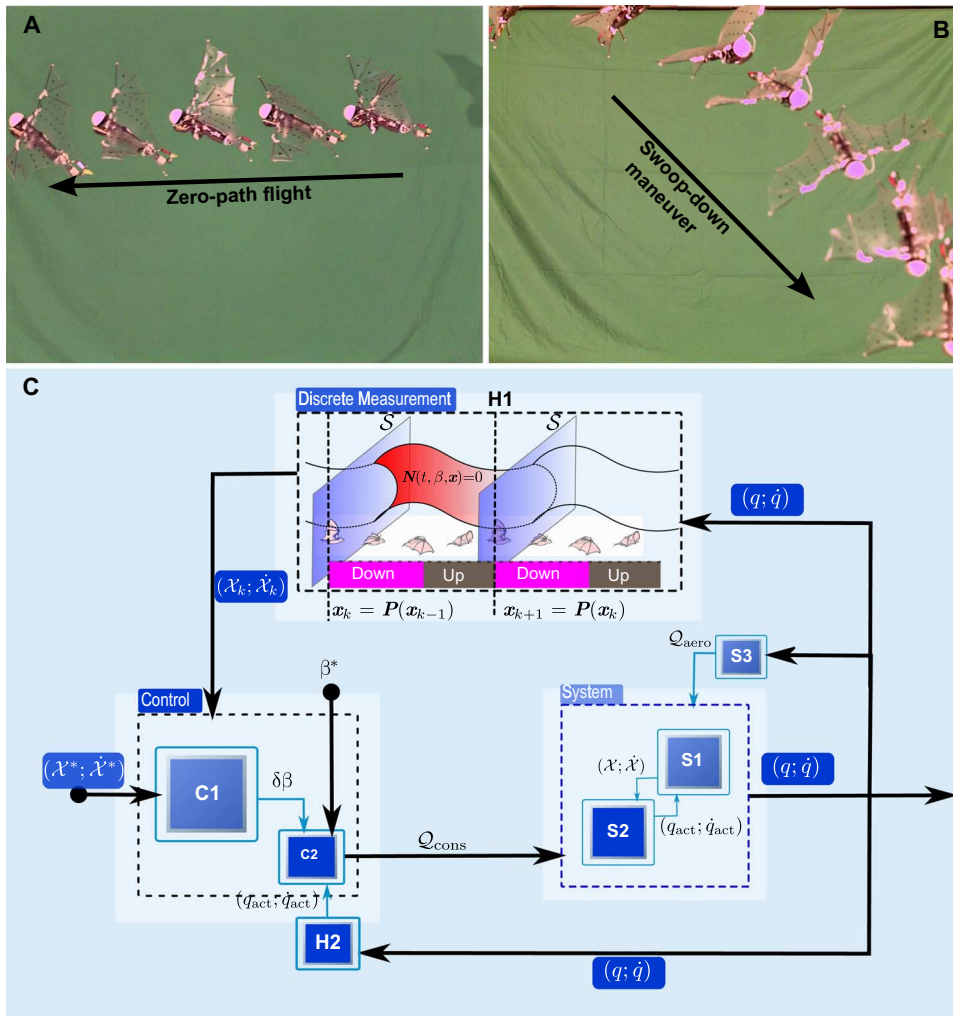
Fig. 4. Untethered flights and controller architecture. (**A**) Snapshots of a zero-path straight flight. (**B**) Snapshots of a diving maneuver. (**C**) The main controller consists of the discrete (C1) and morphing controllers (C2). The discrete and morphing controllers are updated through sensor measurements H1 and H2 at 10 and 100 Hz, respectively. The subsystems S1, S2, and S3 are the underactuated, actuated, and aerodynamic parts [see Materials and Methods and (40)].

finite-state nonlinear optimizer to shape these constraints subject to a series of predefined conditions (40).

The stability of the designed periodic solutions can be checked by inspecting the eigenvalues of the monodromy matrix [Eq. 22 in (40)] after defining a Poincaré map **P** and a Poincaré section $\mathcal{S}$ (40). We computed the monodromy matrix by using a central difference scheme. We perturbed our system states around the equilibrium point at the beginning of the flapping cycle and then integrated the system dynamics given in Eqs. 10 and 16 throughout one flapping cycle.

To stabilize the designed periodic solution, we augmented the desired trajectory $\mathbf{r}_{\mathrm{des}}$ with a correction term $\mathbf{r}_{\mathrm{corr}} = (\partial \mathbf{r}_{\mathrm{des}}/\partial \beta)\delta\beta$, where $\delta\beta$ is computed by Eq. 7. The Poincaré return map takes the robot states $\mathbf{q}_k$ and $\dot{\mathbf{q}}_k$ (the Euler angles roll, pitch, and yaw and their rates) at the beginning of the kth flapping cycle and leads to the states at the beginning of the next flapping cycle,

$$\begin{bmatrix} \mathbf{q}_{k+1} \\ \dot{\mathbf{q}}_{k+1} \end{bmatrix} = \mathbf{P}(\mathbf{q}_k, \dot{\mathbf{q}}_k, \mathbf{r}_{\mathrm{corr}}) \quad (4)$$

We linearized the map **P** at $\mathcal{S}$, resulting in a dynamic system that describes the periodic behavior of the system at the beginning of each flapping cycle

$$\begin{bmatrix} \delta\mathbf{q}_{k+1} \\ \delta\dot{\mathbf{q}}_{k+1} \end{bmatrix} = \begin{bmatrix} \dfrac{\partial \mathbf{P}}{\partial \mathbf{q}}(\mathbf{q}^*) & \dfrac{\partial \mathbf{P}}{\partial \dot{\mathbf{q}}}(\dot{\mathbf{q}}^*) \end{bmatrix}$$
$$\times \begin{bmatrix} \delta\mathbf{q}_k \\ \delta\dot{\mathbf{q}}_k \end{bmatrix} + \dfrac{\partial \mathbf{P}}{\partial \boldsymbol{\beta}}(\boldsymbol{\beta}^*)\delta\boldsymbol{\beta}_k \quad (5)$$

where (*) denotes the equilibrium points and ($\delta\mathbf{q}; \delta\dot{\mathbf{q}}$) denotes deviations from the equilibrium points. The changes in the kinematic parameters are denoted by $\delta\boldsymbol{\beta}$. Here, the stability analysis of the periodic trajectories of the bat robot is relaxed to the stability analysis of the equilibrium of the linearized Poincaré return map on $\mathcal{S}$ [see (40)]. As a result, classical feedback design tools can be applied to stabilize the system. We computed a constant state feedback gain matrix $\mathbf{K}_{\mathcal{S}}$ such that the closed-loop linearized map is exponentially stable:

$$\mathrm{eig}\left(\begin{bmatrix} \dfrac{\partial \mathbf{P}}{\partial \mathbf{q}}(\mathbf{q}^*) & \dfrac{\partial \mathbf{P}}{\partial \dot{\mathbf{q}}}(\dot{\mathbf{q}}^*) \end{bmatrix} + \dfrac{\partial \mathbf{P}}{\partial \boldsymbol{\beta}}(\boldsymbol{\beta}^*)\mathbf{K}_{\mathcal{S}} \right) < 1 \quad (6)$$

We used this state feedback policy at the beginning of each flapping cycle to update the kinematic parameters as follows:

$$\delta\boldsymbol{\beta}_k = \mathbf{K}_{\mathcal{S}} \begin{bmatrix} \delta\mathbf{q}_k \\ \delta\dot{\mathbf{q}}_k \end{bmatrix}. \quad (7)$$

In Fig. 4C, the controller architecture is shown. The controller consists of two parts: (i) the discrete controller that updates the kinematic
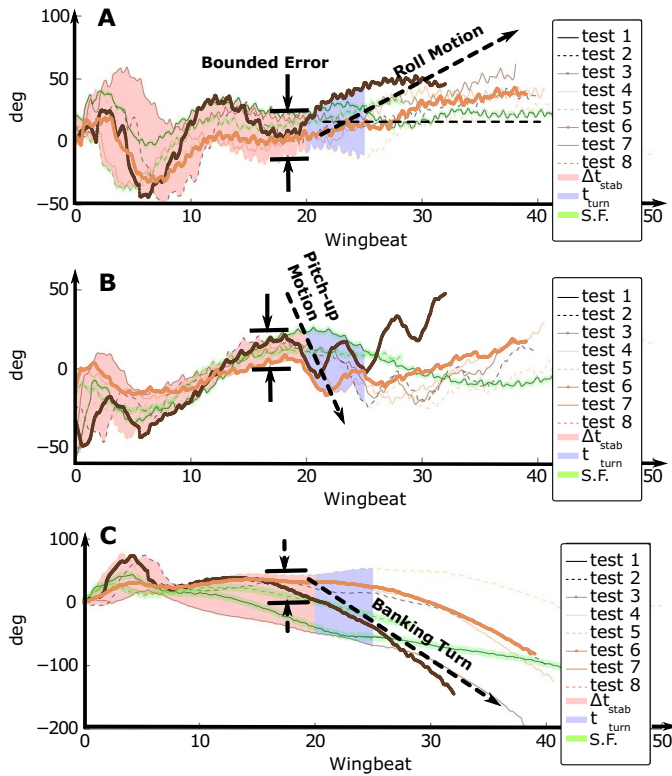
explained mathematically in (40), which reflects two loops made by (p_0-p_1-p_2) and (p_1-p_3-p_4-p_5), as shown in Fig. 3B. We used these configuration variables to develop B2's nonlinear dynamic model and predefined actuator trajectories; see Materials and Methods and (40).

Now, the virtual constraints are given by

$$\mathbf{N}(t, \boldsymbol{\beta}, \mathbf{q}_{\mathrm{act}}) = \mathbf{q}_{\mathrm{act}} - \mathbf{r}_{\mathrm{des}}(t, \boldsymbol{\beta}) \quad (3)$$

where $\mathbf{r}_{\mathrm{des}}$ is the time-varying desired trajectory associated with the actuated coordinates, t is time, and $\boldsymbol{\beta}$ is the vector of the wing kinematic parameters explained in Materials and Methods. Once the virtual constraints (**N**) are enforced, the posture of B2 varies because the actuated portion of the system now implicitly follows the time-varying trajectory $\mathbf{r}_{\mathrm{des}}$. To design $\mathbf{r}_{\mathrm{des}}$, we precomputed the time evolution of B2's joint trajectories for $\mathbf{N} = 0$. We applied numerically stable approaches to guarantee that these trajectory evolutions take place on a constraint manifold (see Materials and Methods). Then, we used a

Fig. 5. The time evolution of the Euler angles roll q_x, pitch q_y, and yaw q_z for eight flight tests is shown. (**A** and **B**) The roll and pitch angles converge to a bounded neighborhood of 0° despite perturbations at the launch moment. The red region represents the time envelope required for vehicle stabilization and is denoted by Δt_{stab}. For all of the flight experiments except the first [denoted by S.F. (straight flight) and highlighted by the green region], a bank turn command was sent at a time within the blue range. Then, the roll and pitch angles start to increase, indicating the beginning of the bank turn. (**C**) The behavior of the yaw angle. In the red region, vehicle heading is stabilized (except flight tests 1 and 4). In the blue region, the vehicle starts to turn toward the right armwing (negative heading rate). This behavior is not seen in the straight flight.

Fig. 6. Armwing joint angle time evolution. Left and right armwing angles q_{FE}^L (**A** and **B**) and q_{FE}^R (**C** and **D**) are shown for eight flight tests. (A and C) Closeup views for the stabilization time envelope. The red region represents the joint movement during the stabilization time envelope. (B and D) After the stabilization time envelope, for all of the flight experiments except the first (highlighted with green), a bank turn command was sent at a time within the blue range.

parameters $\boldsymbol{\beta}$ at ≈10 Hz and (ii) the morphing controller that enforces the predefined trajectories $\mathbf{r}_{des}$ and loops at 100 Hz.

Next, we used joint movements (q_{FE}^R, q_{FE}^L, q_{DV}^R, and q_{DV}^L) to flex (extend) the armwings or ascend (descend) the legs and reconstructed two flight maneuvers: (i) a banking turn and (ii) a swoop maneuver. These joint motions were realized by modifying the term b_i in the actuator-desired trajectories (Eq. 12 in Materials and Methods).

Banking turn maneuver

We performed extensive untethered flight experiments in a large indoor space (Stock Pavilion at the University of Illinois in Champaign-Urbana) where we could use a net (30 m by 30 m) to protect the sensitive electronics of B2 at the moment of landing. The flight arena was not equipped with any motion capture system. Although the vehicle landing position was adjusted by an operator to secure landings within the area, which is covered by the net, we landed outside the net many times. The launching task was performed by a human operator, thereby adding to the degree of inconsistency of the launches.

In all of these experiments, at the launch moment, the system reached its maximum flapping speed (≈10 Hz). In Fig. 5A, the time evolution of the roll angle q_x sampled at 100 Hz is shown. The hand
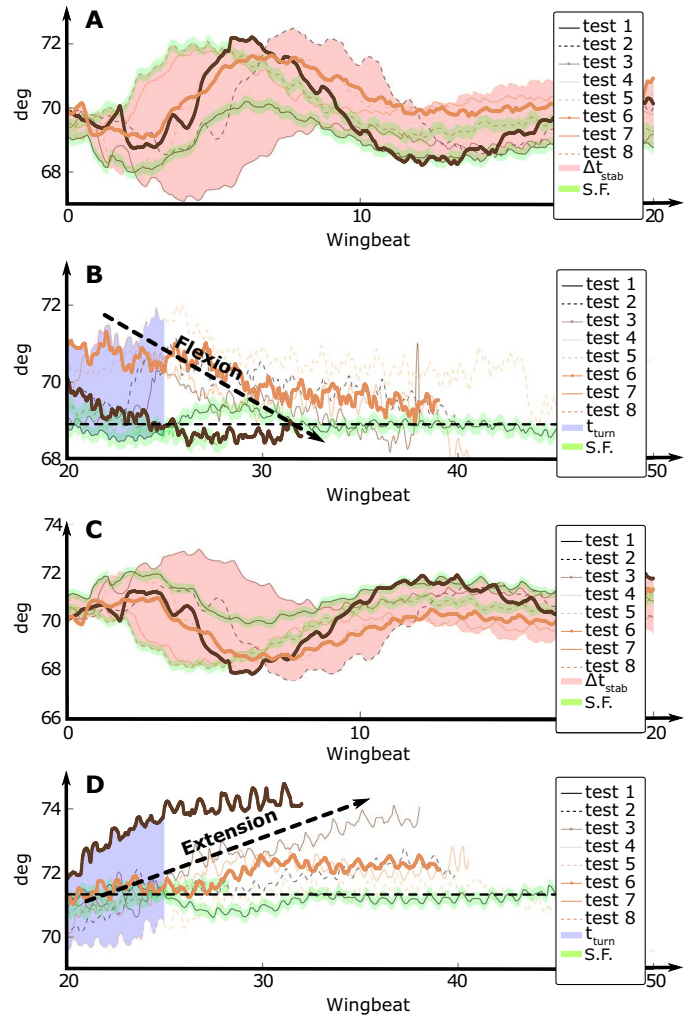
launch introduced initial perturbations, which considerably affected the first 10 wingbeats. Despite the external perturbations of the launch moment, the vehicle stabilized the roll angle within 20 wingbeats. This time envelope is denoted by Δt_{stab} and is shown by the red region. Then, the operator sends a turn command, which is shown by the blue region. Immediately after sending the command, the roll angle increased, indicating a turn toward the right wing. The first flight test, which is shown in a solid black line and highlighted with green, does not follow the increase trend because the turn command was not applied for comparison purposes in this experiment.

In Figs. 6 and 7, the morphing joint angles q_{FE}^L, q_{FE}^R, q_{DV}^L, and q_{DV}^R for these flight tests are reported. These joint angles were recorded by the onboard Hall effect sensors and were sampled at 100 Hz. As Fig. 6 (A to D) suggests, the controller achieves positive roll angle in the blue region by flexing the right armwing and extending the left armwing.

In Fig. 5 (B and C), the time evolutions of the Euler angles q_y and q_z are shown. Like the roll angle, the pitch angle was settled within a
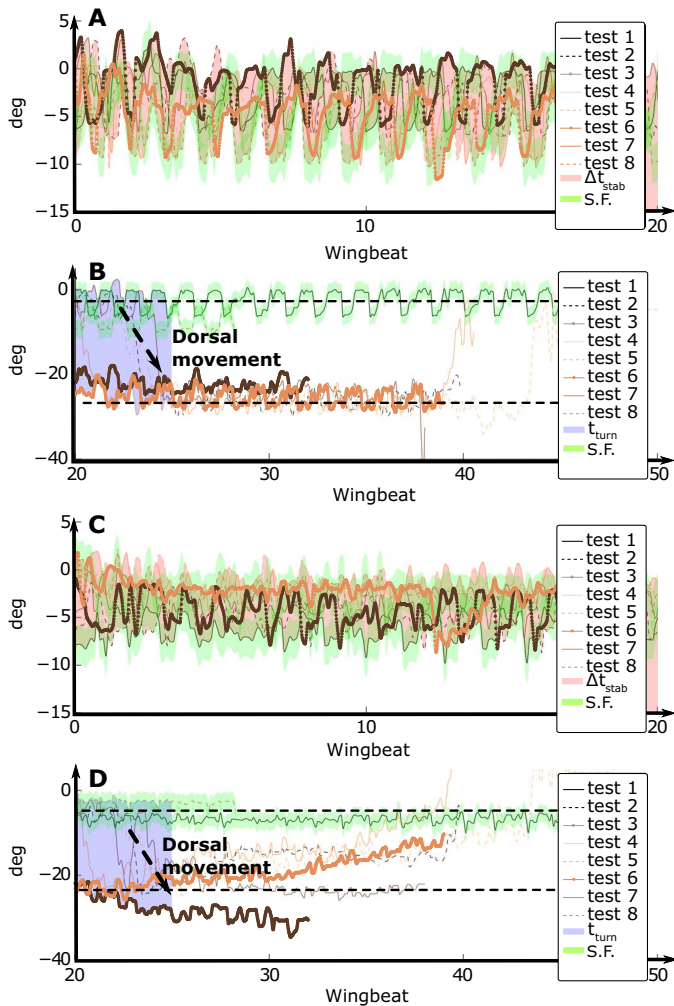
Fig. 7. Leg joint angle time evolution. Left and right leg angles q_{DV}^L (**A** and **B**) and q_{DV}^R (**C** and **D**) are shown for eight flight tests. (A and C) Closeup views for the stabilization time envelope. (B and D) After the stabilization time envelope, the dorsal movement of the legs are applied to secure a successful belly landing. This dorsal movement can cause pitch-up artifacts, which are extremely nonlinear.

bounded neighborhood of 0 in the red region. At the moment of the banking turn (blue region), pitch-up artifacts appeared because of extreme nonlinear couplings between the roll and pitch dynamics. In addition, these pitch-ups, to some extent, are the result of the dorsal movement of the legs, which are applied to secure a successful belly landing (see Fig. 7, A to D). The straight flight pitch angle behaved differently because there were no sharp rises in the pitch angle in the blue region. In Fig. 5C, it is easy to observe that for all of the flight tests (except the straight flight), the rate of changes in the heading angle increased after the turn command is applied, suggesting the onset of the bank turning.

Diving maneuver

Next, a sharp diving maneuver, which is performed by bats when pursuing their prey, was reconstructed. Insectivorous echolocating bats face a sophisticated array of defenses used by their airborne prey. One such insect defense is the ultrasound-triggered dive, which

is a sudden, rapid drop in altitude, sometimes all the way to the ground.

We tried to reconstruct this maneuver by triggering a sharp pitch-down motion at mid-flight. After launching the robot, the operator sent the command, which resulted in a sharp ventral movement of the legs (shown in Fig. 8C). Meanwhile, the armwings are stretched (shown in Fig. 8B). In Fig. 8A, a sharp rise of the pitch angle is noticeable. The vehicle swooped and reached a peak velocity of about 14 m/s. This extreme agile maneuver testifies to the level of attitude instability in B2.

Flight characteristics

B2's flight characteristics are compared with *Rousettus aegyptiacus* flight information from (41). *R. aegyptiacus* flight information corresponds to the flight speed U that is within the range of 3 to 5 m/s. B2's morphological details, which are presented in table S1, are used to compute B2's flight characteristics. According to Rosén *et al.* (28), the arc length traveled by the wingtip s_{tip} is given by $s_{tip} = 2\psi b_s$, where ψ and b_s are the flapping stroke angle and wingspan, respectively ($s_{tip,B2} = 0.48$ and $s_{tip,Rous.} = 0.36$). A motion capture system (shown in fig. S3) was used to register the position coordinates p_x and p_y for four untethered flight tests (see fig. S2). The flight speed was calculated by taking the time derivative of p_x and p_y. We considered the average flight speed $\bar{U}_{B2} = 5.6$ m/s in the succeeding calculations.

The measure K (28), which is similar to the reduced frequency and is computed on the basis of the wingtip speed, is given by $K = s_{tip}/t_f/U$, where t_f is the time span of a single wingbeat ($K_{B2} = 0.86$ and $K_{Rous.} = 0.81$). Subsequently, the advance ratio J is equal to the inverse of the measure K ($J_{B2} = 1.16$ and $J_{Rous.} = 1.22$). The wing loading Q_s is given by $Q_s = M_b g/S_{max}$ (41), where M_b is the total body mass, g is the gravitational constant, and S_{max} is the maximum wing area ($Q_{s,B2} = 13$ N/m^2 and $Q_{s,Rous.} = 11$ N/m^2).

The Strouhal number St is given by $St = \Delta z_{tip}/t_f/U$ (41), where Δz_{tip} is the vertical displacement of the wingtip with respect to the shoulder (28) ($St_{B2} = 0.43$ and $St_{Rous.} = 0.4 - 0.6$). Last, the nominal coefficient of lift C_l is computed. The coefficient is given by $C_l = 2F_{vert}/(\rho_{air} V_c^2 S_{max})$ from (41), where ρ_{air} is the density of dry air, V_c is the velocity of the carpus (see Fig. 3B), and F_{vert} is the magnitude of the vertical lift force (see fig. S4). We measured F_{vert} by installing the robot on top of a miniature load cell, which is inside a wind tunnel. The wind tunnel is programmed to sustain air velocity at 4 to 6 m/s ($C_{l,B2} = 0.8$ and $C_{l,Rous.} = 1.0$).

CONCLUSION

Bats are known to demonstrate exceptionally agile maneuvers thanks to many joints that are embedded in their flight mechanism, which synthesize sophisticated and functionally versatile dynamic wing conformations. Bats represent a unique solution to the challenges of maneuverable flapping flight and provide inspiration for vehicle design at bat-length scales.

The difficulties associated with reconstructing bat-inspired flight are exacerbated by the inherent complexities associated with the design of such bat robots. Consequently, we have identified and implemented the most important wing joints by means of a series of mechanical constraints and a feedback control design to control the six-DOF flight motion of the bat robot called B2.

The main results of this study are fourfold. First, for robotics, this work demonstrates the synergistic design and flight control of an aerial robot with dynamic wing conformations similar to those of
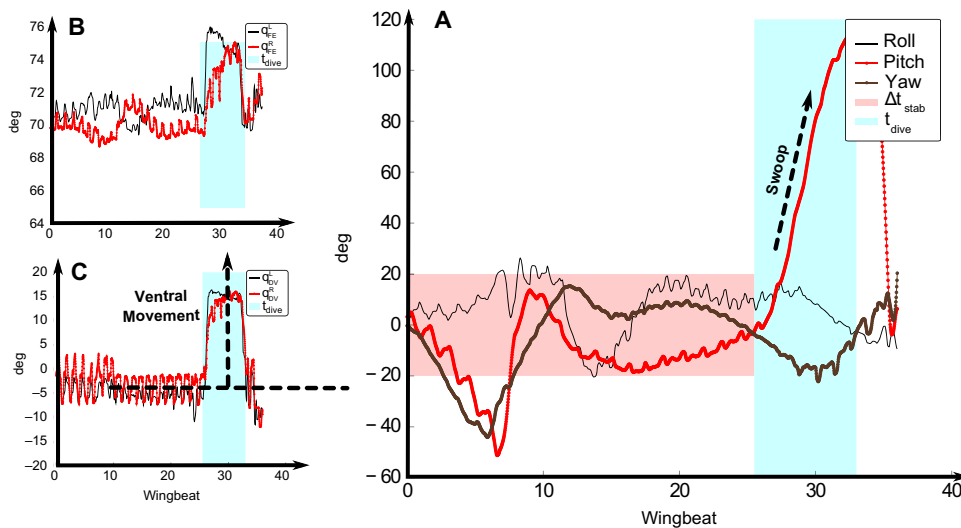
Fig. 8. Joint angle evolution during swooping down. (**A**) The time evolution of the Euler angles during the diving maneuver. (**B**) Armwing joint angles. (**C**) Leg joint angles. The red region indicates the stabilization time envelope; the light blue region indicates the dive time span.

biological bats. Conventional flapping wing platforms have wings with few joints, which can be conceptualized as rigid bodies. These platforms often use conventional fixed-wing airplane control surfaces (e.g., rudders, ailerons, etc.); therefore, these robots are not suitable for examining the flight mechanisms of biological counterparts with nontrivial morphologies.

This work has demonstrated several autonomous flight maneuvers (zero-path flight, banking turn, and diving) of a self-contained robotic platform that has fundamentally distinguished control arrays in comparison to existing flapping robots. B2 uses a morphing skeleton array wherein the use of a silicone-based skin enables the robot to morph its articulated structure in midair without losing an effective and smooth aerodynamic surface. This morphing property will not be realized with conventional fabrics (e.g., nylon and Mylar) that are primarily used in flapping wing research.

Next, for dynamics and control, this work applies the notion of stable periodic orbits to study aerial locomotion of B2, whose unstable flight dynamics are aggravated by the flexibility of the wings. The technique used in the paper can simplify stability analysis by establishing equivalence between the stability of a periodic orbit and a linearized Poincaré map.

Third, this work introduces a design scheme (as shown in Fig. 1) to mimic the key flight mechanisms of biological counterparts. There is no well-established methodology for reverse engineering the sophisticated locomotion of biological counterparts. These animals have several active and passive joints that make it impractical to incorporate all of them in the design. The framework that is introduced in this study accommodates the key DOFs of bat wings and legs in a 93-g flying robot with tight payload and size restrictions. These DOFs include the retraction-protraction of the shoulders, flexion-extension of the elbows, abduction-adduction of the wrists, and dorsoventral movement of the legs. The design framework is staged in two steps: introducing mechanical constraints motivated by PCA of bat flight kinematics and designing virtual constraints motivated by holonomically constrained mechanical systems.

Last but not least, this research contributes to biological studies on bat flight. The existing methods for biology rely on vision-based motion

capture systems that use high-speed imaging sensors to record the trajectory of joints and limbs during bat flight. Although these approaches can effectively analyze the joint kinematics of bat wings in flight, they cannot help understand how specific DOFs or specific wing movement patterns contribute to a particular flight maneuver of a bat. B2 can be used to reconstruct flight maneuvers of bats by applying wing movement patterns observed in bat flight, thereby helping us understand the role of the dominant DOFs of bats. In this work, we have demonstrated the effectiveness of using this robot to reproduce flight maneuvers such as straight flight, banking turn, and diving flight. Motivated by previous biological studies such as that by Gardiner *et al.* (*42*), which inspects the role of the legs in modulating the pitch movement of bat flight, we have successfully implemented the dorsoventral movement control of the legs of B2 to produce a sharp diving maneuver or to maintain a straight path. Furthermore, in this work, bank turn maneuvers of bats (*23*) have been successfully reconstructed by controlling asymmetric wing folding of the two main wings. The self-sufficiency of an autonomous robotic platform in sensing, actuation, and computation permits extensive analysis of dynamic system responses. In other words, thorough and effective inspection of the key DOFs in bat flight is possible by selectively perturbing these joint angles of the robot and analyzing the response. It is the presence of several varying parameters in bat flight kinematics that hinders such a systematic analysis. Consequently, we envision the potential applications of our robotic platform as an important tool for studying bat flight in the context of robotic-inspired biology.

MATERIALS AND METHODS
Nonlinear dynamics
The mathematical dynamic model of B2 is developed using the Lagrange method (*36*) after computing kinetic and potential energies. Rotary and translational kinetic energies are evaluated after defining the position and attitude of the body with respect to the inertial frame. Euler angles are used to define the attitude of the robot with respect to the inertial frame, whereas body coordinate frames, which are attached to the wings, define the wing movements with respect to the body coordinate frame.

Modeling assumptions.
The following assumptions are made during the nonlinear dynamic modeling:

(1) Wing inertial forces are considered because the wings are not massless.

(2) There is no spanwise and chordwise flexibility in the wings; that is, it is a rigid flapping wing aircraft. Therefore, there is no flexibility-induced phase difference between flapping and feathering motions, and no degrees of underactuation are introduced as a result of passive phase difference between the flapping and feathering (pitch) motions.

(3) Strip theory (*43*) is used for computing aerodynamic forces and moments.

(4) The aerodynamic center is assumed to be located at the quarter-chord point (*31*), and the aerodynamic forces, which act on the aerodynamic center, include the lift and drag forces.

Method of Lagrange.
During free-fall ballistic motions, B2 with its links and joints represents an open kinematic chain that evolves under the influence of gravitational and external aerodynamic forces. We used the method of Lagrange to mathematically define this dynamics. This open kinematic chain is uniquely determined with the fuselage Euler angles roll, pitch, and yaw (q_x; q_y; q_z); fuselage center of mass (CoM) positions (p_x; p_y; p_z); and morphing joint angles $\mathbf{q}_{morph}$ defined in Eq. 1. Therefore, the robot's configuration variable vector is

$$\mathbf{q} = (q_x; q_y; q_z; p_x; p_y; p_z; \mathbf{q}_{morph}) \in \mathcal{Q} \qquad (8)$$

where $\mathcal{Q}$ is the robot's configuration variable space. We derived Lagrange equations after computing the total energy of the free open kinematic chain as the difference between the total kinetic energy and the total potential energy. Following Hamilton's principle of least action, the equations of motion for the open kinematic chain with ballistic motions are given by:

$$\mathcal{M}(\mathbf{q})\ddot{\mathbf{q}} + \mathcal{C}(\mathbf{q}, \dot{\mathbf{q}})\dot{\mathbf{q}} + \mathcal{G}(\mathbf{q}) = \mathcal{Q}_{gen} \qquad (9)$$

where $\mathcal{M}$, $\mathcal{C}$, and $\mathcal{G}$ denote the inertial matrix, the Coriolis matrix, and the gravity vector, respectively. The generalized forces $\mathcal{Q}_{gen}$, which reflect the role of aerodynamic forces as well the action of several morphing motors in B2, are described in (*40*).

Virtual constraints and offline actuator trajectory design
For wing articulations, we use a framework based on defining a set of parameterized and time-varying holonomic constraints (*37*, *38*). This method permits shaping of the overall system dynamics through such constraints. These holonomic constraints control the posture of the articulated flight mechanism by driving the actuated portion of the system and take place through the action of the servo actuators that are embedded in the robot.

We partitioned the configuration variable vector $\mathbf{q}$ into the actuated coordinates $\mathbf{q}_{act}$ and the remaining coordinates $\mathcal{X}$, which includes Euler angles and body CoM positions. The dynamics (Eq. 9) are rewritten as

$$\begin{bmatrix} \mathcal{M}_{11} & \mathcal{M}_{12} \\ \mathcal{M}_{21} & \mathcal{M}_{22} \end{bmatrix} \begin{bmatrix} \ddot{\mathcal{X}} \\ \ddot{\mathbf{q}}_{act} \end{bmatrix} + \begin{bmatrix} \mathcal{C}_{11} & \mathcal{C}_{12} \\ \mathcal{C}_{21} & \mathcal{C}_{22} \end{bmatrix} \begin{bmatrix} \dot{\mathcal{X}} \\ \dot{\mathbf{q}}_{act} \end{bmatrix}$$
$$+ \begin{bmatrix} \mathcal{G}_1 \\ \mathcal{G}_2 \end{bmatrix} = \mathcal{Q}_{cons} + \mathcal{Q}_{aero}. \qquad (10)$$

In the equation above, $\mathcal{M}_{11}$, $\mathcal{M}_{12}$, $\mathcal{M}_{21}$, $\mathcal{M}_{22}$, $\mathcal{C}_{11}$, $\mathcal{C}_{12}$, $\mathcal{C}_{21}$, and $\mathcal{C}_{22}$ are block matrices; $\mathcal{Q}_{cons}$ and $\mathcal{Q}_{aero}$ are two components of the generalized forces (*40*). The nonlinear system in Eq. 10 shows that the actuated and unactuated dynamics are coupled by the inertial, Coriolis, gravity, and aerodynamic terms.

The actuated dynamics represent the servo actuators in the robot. The action of these actuators is described by introducing parameterized and time-varying holonomic constraints into the dynamic system. To shape the actuated coordinates, we defined a constraint manifold, and we used numerically stable approaches to enforce the evolution of the

trajectories on this manifold. Thereafter, a finite-state nonlinear optimizer shapes these constraints.

The servo actuators move the links to the desired positions. This is similar to the behavior of a holonomically constrained mechanical system and, mathematically speaking, is equivalent to the time evolution of the system dynamics given by Eq. 10 over the manifold

$$\mathcal{H} := \{(\mathbf{q}; \dot{\mathbf{q}}) \in T\mathcal{Q} | \mathbf{N} = 0\} \qquad (11)$$

where $\mathbf{N}$ is the constraint equation and is given by $\mathbf{N}(t, \boldsymbol{\beta}, \mathbf{q}_{act}) = \mathbf{q}_{act} - \mathbf{r}_{des}(t, \boldsymbol{\beta})$. In the constraint equation, $\mathbf{r}_{des}$ is the vector of the desired trajectories for the actuated coordinates $\mathbf{q}_{act}$ and is given by

$$\mathbf{r}_{des}^i(t, \boldsymbol{\beta}) = a_i \cos(\omega t + \phi_i) + b_i, \quad i \in \left\{y_{spindle}^R, q_{DV}^R, y_{spindle}^L, q_{DV}^L, q_{FL}\right\} \qquad (12)$$

where t denotes time and $\boldsymbol{\beta} = \{\omega, \phi_i, a_i, b_i\}$ parameterizes the periodic actuator trajectories that define the wing motion. These parameters are the control input to the system. Imposing the constraint equations to the system dynamics (Eq. 10) at only the acceleration level will lead to numeric problems owing to the difficulties of obtaining accurate position and velocity initial values (*44*). In addition, numeric discretization errors will be present during the process of integration, and the constraints will not be satisfied. Therefore, the constraints in position and velocity levels are also considered (*45*)

$$\ddot{\mathbf{N}} + \kappa_1 \dot{\mathbf{N}} + \kappa_2 \mathbf{N} = 0. \qquad (13)$$

where $\kappa_{1,2}$ are two constant matrices and

$$\ddot{\mathbf{N}} = \frac{\partial^2 \mathbf{N}}{\partial t^2} + \frac{\partial}{\partial \mathbf{q}_{act}} \left(\frac{\partial \mathbf{N}}{\partial \mathbf{q}_{act}} \dot{\mathbf{q}}_{act} \right) \dot{\mathbf{q}}_{act} + \frac{\partial \mathbf{N}}{\partial \mathbf{q}_{act}} \ddot{\mathbf{q}}_{act}, \qquad (14)$$

and

$$\dot{\mathbf{N}} = \frac{\partial \mathbf{N}}{\partial t} + \frac{\partial \mathbf{N}}{\partial \mathbf{q}_{act}} \dot{\mathbf{q}}_{act}. \qquad (15)$$

Substituting Eqs. 14 and 15 to Eq. 13 gives $\ddot{\mathbf{q}}_{act}$. Now, interlocking Eq. 10 and $\ddot{\mathbf{q}}_{act}$ forms the following system of ordinary differential equations on a parameterized manifold:

$$\begin{cases} \begin{bmatrix} \ddot{\mathcal{X}} \\ \ddot{\mathbf{q}}_{act} \end{bmatrix} = \left(\begin{bmatrix} \mathcal{M}_{11} & \mathcal{M}_{12} \\ \mathcal{M}_{21} & \mathcal{M}_{22} \end{bmatrix} \right)^{-1} \left(- \begin{bmatrix} \mathcal{C}_{11} & \mathcal{C}_{12} \\ \mathcal{C}_{21} & \mathcal{C}_{22} \end{bmatrix} \begin{bmatrix} \dot{\mathcal{X}} \\ \dot{\mathbf{q}}_{act} \end{bmatrix} - \begin{bmatrix} \mathcal{G}_1 \\ \mathcal{G}_2 \end{bmatrix} + \mathcal{Q}_{cons} + \mathcal{Q}_{aero}(\mathbf{q}, \dot{\mathbf{q}}) \right) \\ \ddot{\mathbf{q}}_{act} = \left(\frac{\partial \mathbf{N}}{\partial \mathbf{q}_{act}} \right)^{-1} \left(-\kappa_1 \dot{\mathbf{N}} - \kappa_2 \mathbf{N} - \frac{\partial^2 \mathbf{N}}{\partial t^2} - \frac{\partial}{\partial \mathbf{q}_{act}} \left(\frac{\partial \mathbf{N}}{\partial \mathbf{q}_{act}} \dot{\mathbf{q}}_{act} \right) \dot{\mathbf{q}}_{act} \right). \end{cases} \qquad (16)$$

Now, the numeric integration of the above differential-algebraic equation (DAE) is possible, and consequently, it is possible to design predefined periodic trajectories for the actuators. In (*40*), we have used finite-state optimization and shooting methods to design periodic solutions for the DAE.

To verify the accuracy of the proposed nonlinear dynamic model in predicting the behavior of the vehicle, we compared the trajectories from eight different flight experiments with the model-predicted trajectories. In fig. S1, the time evolution of the pitch angle q_y and pitch rate angle $\dot{q}_y$ is shown.

SUPPLEMENTARY MATERIALS

Supplementary Text
Fig. S1. Nonlinear model verification.
Fig. S2. Flight speed measurements.
Fig. S3. Motion capture system.
Fig. S4. Wind tunnel measurements.
Table S1. B2's morphological details.
Movie S1. Membrane.
Movie S2. Articulated skeleton.
Movie S3. Straight flights.
Movie S4. Swoop maneuver.
Movie S5. Banking turn maneuver.
References (46–59)

REFERENCES AND NOTES

1. K. Ma, P. Chirarattanon, S. Fulsler, R. Wood, Controlled flight of a biologically inspired, insect-scale robot. *Science* **340**, 603–607 (2013).

2. A. Paranjape, S.-J. Chung, J. Kim, Novel dihedral-based control of flapping-wing aircraft with application to perching. *IEEE Trans. Robot.* **29**, 1071–1084 (2013).

3. J. W. Gerdes, S. K. Gupta, S. A. Wilkerson, A review of bird-inspired flapping wing miniature air vehicle designs. *J. Mech. Robot.* **4**, 021003 (2012).

4. J. W. Bahlman, S. M. Swartz, K. S. Breuer, Design and characterization of a multi-articulated robotic bat wing. *Bioinspir. Biomim.* **8**, 016009 (2013).

5. S.-J. Chung, M. Dorothy, Neurobiologically inspired control of engineered flapping flight. *J. Guid. Control Dyn.* **33**, 440–453 (2010).

6. D. K. Riskin, D. J. Willis, J. Iriarte-Díaz, T. L. Hedrick, M. Kostandov, J. Chen, D. H. Laidlaw, K. S. Breuer, S. M. Swartz, Quantifying the complexity of bat wing kinematics. *J. Theor. Biol.* **254**, 604–615 (2008).

7. S. M. Swartz, J. Iriarte-Diaz, D. K. Riskin, A. Song, X. Tian, D. J. Willis, K. S. Breuer, Wing structure and the aerodynamic basis of flight in bats, paper presented at 45th AIAA Aerospace Sciences Meeting and Exhibit, 8 to 11 January 2007, Reno, NV (2007); http://arc.aiaa.org/doi/abs/10.2514/6.2007-42.

8. A. Azuma, *The Biokinetics of Flying and Swimming* (Springer Science & Business Media, 2012).

9. X. Tian, J. Iriarte-Diaz, K. Middleton, R. Galvao, E. Israeli, A. Roemer, A. Sullivan, A. Song, S. Swartz, K. Breuer, Direct measurements of the kinematics and dynamics of bat flight. *Bioinspir. Biomim.* **1**, S10–S18 (2006).

10. X. Deng, L. Schenato, W. C. Wu, S. S. Sastry, Flapping flight for biomimetic robotic insects: Part I-system modeling. *IEEE Trans. Robot.* **22**, 776–788 (2006).

11. X. Deng, L. Schenato, S. S. Sastry, Flapping flight for biomimetic robotic insects: Part II-flight control design. *IEEE Trans. Robot.* **22**, 789–803 (2006).

12. R. J. Wood, S. Avadhanula, E. Steltz, M. Seeman, J. Entwistle, A. Bachrach, G. Barrows, S. Sanders, R. S. Fearing, Enabling technologies and subsystem integration for an autonomous palm-sized glider. *IEEE Robot. Autom. Mag.* **14**, 82–91 (2007).

13. R. J. Wood, The first takeoff of a biologically inspired at-scale robotic insect. *IEEE Trans. Robot.* **24**, 341–347 (2008).

14. D. B. Doman, C. Tang, S. Regisford, Modeling interactions between flexible flapping-wing spars, mechanisms, and drive motors. *J. Guid. Control Dyn.* **34**, 1457–1473 (2011).

15. I. Faruque, J. Sean Humbert, Dipteran insect flight dynamics. Part 1 Longitudinal motion about hover. *J. Theor. Biol.* **264**, 538–552 (2010).

16. J. Dietsch, Air and sea robots add new perspectives to the global knowledge base. *IEEE Robot. Autom. Mag.* **18**, 8–9 (2011).

17. S. A. Combes, T. L. Daniel, Shape, flapping and flexion: Wing and fin design for forward flight. *J. Exp. Biol.* **204**, 2073 (2001).

18. S. A. Combes, T. L. Daniel, Into thin air: Contributions of aerodynamic and inertial-elastic forces to wing bending in the hawkmoth *Manduca sexta*. *J. Exp. Biol.* **206**, 2999–3006 (2003).

19. S. Lupashin, A. Schöllig, M. Sherback, R. D'Andrea, A simple learning strategy for high-speed quadrocopter multi-flips, in *Proceedings of the IEEE International Conference on Robotics and Automation (ICRA)* (IEEE, 2010), pp. 1642–1648.

20. N. Michael, D. Mellinger, Q. Lindsey, V. Kumar, The grasp multiple micro-UAV testbed. *IEEE Robot. Autom. Mag.* **17**, 56–65 (2010).

21. H. D. Aldridge, Kinematics and aerodynamics of the greater horseshoe bat, *Rhinolophus ferrumequinum*, in horizontal flight at a various flight speeds. *J. Exp. Biol.* **126**, 479–497 (1986).

22. H. D. Aldridge, Body accelerations during the wingbeat in six bat species: The function of the upstroke in thrust generation. *J. Exp. Biol.* **130**, 275–293 (1987).

23. U. M. Norberg, Some advanced flight manoeuvres of bats. *J. Exp. Biol.* **64**, 489–495 (1976).

24. C. Chevallereau, G. Abba, Y. Aoustin, F. Plestan, E. R. Westervelt, C. Canudas-de-wit, J. W. Grizzle, Rabbit: A testbed for advanced control theory. *IEEE Control Syst. Mag.* **23**, 57–79 (2003).

25. Y. P. Ivanenko, A. d'Avella, R. E. Poppele, F. Lacquaniti, On the origin of planar covariation of elevation angles during human locomotion. *J. Neurophysiol.* **99**, 1890–1898 (2008).

26. T. Chau, A review of analytical techniques for gait data. Part 1: Fuzzy, statistical and fractal methods. *Gait Posture* **13**, 49–66 (2001).

27. G. Cappellini, Y. P. Ivanenko, R. E. Poppele, F. Lacquaniti, Motor patterns in human walking and running. *J. Neurophysiol.* **95**, 3426–3437 (2006).

28. M. Rosén, G. Spedding, A. Hedenström, The relationship between wingbeat kinematics and vortex wake of a thrush nightingale. *J. Exp. Biol.* **207**, 4255–4268 (2004).

29. N. A. Bernstein, *The Coordination and Regulation of Movements* (Pergamon Press, 1967).

30. J. Hoff, A. Ramezani, S.-J. Chung, S. Hutchinson, Synergistic design of a bio-inspired micro aerial vehicle with articulated wings. *Proc. Rob. Sci. Syst.* 10.15607/RSS.2016.XII.009 (2016).

31. A. L. Thomas, G. K. Taylor, Animal flight dynamics I. Stability in gliding flight. *J. Theor. Biol.* **212**, 399–424 (2001).

32. W. Maybury, J. Rayner, L. B. Couldrick, Lift generation by the avian tail. *Proc. Biol. Sci.* **268**, 1443–1448 (2001).

33. J. A. Cheney, D. Ton, N. Konow, D. K. Riskin, K. S. Breuer, S. M. Swartz, Hindlimb motion during steady flight of the lesser dog-faced fruit bat, *Cynopterus brachyotis*. *PLOS ONE* **9**, e98093 (2014).

34. A. Ramezani, X. Shi, S.-J. Chung, S. Hutchinson, Bat Bot (B2), A biologically inspired flying machine, in *Proceedings of the IEEE International Conference on Robotics and Automation (ICRA)* (IEEE, 2016), pp. 3219–3226.

35. H. Tanaka, H. Okada, Y. Shimasue, H. Liu, Flexible flapping wings with self-organized microwrinkles. *Bioinspir. Biomim.* **10**, 046005 (2015).

36. A. Ramezani, X. Shi, S.-J. Chung, S. Hutchinson, Lagrangian modeling and flight control of articulated-winged bat robot, in *Proceedings of the 2015 IEEE/RSJ International Conference on Intelligent Robots and Systems (IROS)* (IEEE, 2015), pp. 2867–2874.

37. C. I. Byrnes, A. Isidori, A frequency domain philosophy for nonlinear systems, in *Proceedings of the IEEE Conference on Decision and Control* (IEEE, 1984), pp. 1569–1573.

38. A. Isidori, C. Moog, On the nonlinear equivalent of the notion of transmission zeros, in *Modelling and Adaptive Control*, C. I. Byrnes, A. Kurzhanski, Eds. (Springer, 1988), pp. 146–158.

39. M. Wolf, L. C. Johansson, R. von Busse, Y. Winter, A. Hedenström, Kinematics of flight and the relationship to the vortex wake of a Pallas' long tongued bat (*Glossophaga soricina*). *J. Exp. Biol.* **213**, 2142–2153 (2010).

40. Materials and methods are available as supplementary materials at the *Science* website.

41. D. K. Riskin, J. Iriarte-Daz, K. M. Middleton, K. S. Breuer, S. M. Swartz, The effect of body size on the wing movements of pteropodid bats, with insights into thrust and lift production. *J. Exp. Biol.* **213**, 4110–4122 (2010).

42. J. D. Gardiner, G. Dimitriadis, J. R. Codd, R. L. Nudds, A potential role for bat tail membranes in flight control. *PLOS ONE* **6**, e18214 (2011).

43. J. D. DeLaurier, An aerodynamic model for flapping-wing flight. *Aeronaut. J.* **97**, 125–130 (1993).

44. U. M. Ascher, H. Chin, L. R. Petzold, S. Reich, Stabilization of constrained mechanical systems with daes and invariant manifolds. *J. Struct. Mech.* **23**, 135–157 (1995).

45. C. Führer, B. J. Leimkuhler, Numerical solution of differential-algebraic equations for constrained mechanical motion. *Numer. Math.* **59**, 55–69 (1991).

46. A. H. Nayfeh, Perturbation methods in nonlinear dynamics, in *Nonlinear Dynamics Aspects of Accelerators. Lecture Notes in Physics,* J. M. Jowett, M. Month, S. Turner, Eds. (Springer, 1986), pp. 238–314.

47. M. Goman, A. Khrabrov, State-space representation of aerodynamic characteristics of an aircraft at high angles of attack. *J. Aircr.* **31**, 1109–1115 (1994).

48. A. A. Paranjape, S.-J. Chung, H. H. Hilton, A. Chakravarthy, Dynamics and performance of tailless micro aerial vehicle with flexible articulated wings. *AIAA J.* **50**, 1177–1188 (2012).

49. H. K. Khalil, J. Grizzle, *Nonlinear Systems* (Prentice Hall, 1996).

50. G. Meurant, *An Introduction to Differentiable Manifolds and Riemannian Geometry*, vol. 120 (Academic Press, 1986).

51. R. R. Burridge, A. A. Rizzi, D. E. Koditschek, Sequential composition of dynamically dexterous robot behaviors. *Int. J. Rob. Res.* **18**, 534–555 (1999).

52. J. B. Dingwell, J. P. Cusumano, Nonlinear time series analysis of normal and pathological human walking. *Chaos* **10**, 848–863 (2000).

53. M. S. Garcia, "Stability, scaling, and chaos in passive-dynamic gait models," thesis, Cornell University, Ithaca, NY (1999).

54. J. Guckenheimer, S. Johnson, *International Hybrid Systems Workshop* (Springer, 1994), pp. 202–225.

55. Y. Hurmuzlu, C. Basdogan, J. J. Carollo, Presenting joint kinematics of human locomotion using phase plane portraits and Poincaré maps. *J. Biomech.* **27**, 1495–1499 (1994).

56. S. G. Nersesov, V. Chellaboina, W. M. Haddad, A generalization of Poincaré's theorem to hybrid and impulsive dynamical systems, in *Proceedings of the American Control Conference* (IEEE, 2002), pp. 1240–1245.

57. T. S. Parker, L. Chua, *Practical Numerical Algorithms for Chaotic Systems* (Springer Science & Business Media, 2012).

58. B. Thuilot, A. Goswami, B. Espiau, Bifurcation and chaos in a simple passive bipedal gait, in *Proceedings of the IEEE International Conference on Robotics and Automation* (IEEE, 1997), pp. 792–798.

59. E. R. Westervelt, J. W. Grizzle, C. Chevallereau, J. H. Choi, B. Morris, *Feedback Control of Dynamic Bipedal Robot Locomotion* (CRC Press, 2007).